Chemical Science

ROYAL SOCIETY OF CHEMISTRY

EDGE ARTICLE

View Article Online
View Journal

Cite this: DOI: 10.1039/d6sc03993f

All publication charges for this article have been paid for by the Royal Society of Chemistry

In situ glycosylation-directed H-aggregation of Type I photosensitizers for synergistic biofilm eradication and promoting diabetic wound healing

Dongmei Xi,*[a] Wencai Jiang,[a] Mengyue Li,[a] Jialu Guo,[a] Pengxiang Wang,[a] Fangqian Yin,[a] Xiaopeng Fan,[a] Ke-Rang Wang,*[a] Wen Sun*[b] and Xiaojun Peng[b]

Biofilm-associated diabetic wound infections pose a major therapeutic challenge. Although photodynamic therapy (PDT) offers an alternative antibacterial strategy, conventional photosensitizers are often limited by inadequate biofilm penetration and poor activity under hypoxic conditions. In this study, we report glycosylated photosensitizers (NBS-Gal and NBS-Lac) that spontaneously form H-aggregates in aqueous media *via* π-stacking. This self-assembly integrates molecular function with nanostructure without requiring auxiliary components and enables robust Type I photodynamic activity. Notably, NBS-Lac exhibits superior H-aggregation, resulting in 2.2-fold and 1.8-fold higher $O_2^{\cdot-}$ generation (after 4 min irradiation) than NBS-NH_2 and NBS-Gal, respectively. The glycosyl moieties enable targeted bacterial recognition through carbohydrate–lectin interactions, while the positive charge on NBS facilitates biofilm penetration *via* electrostatic interactions. NBS-Lac achieves 100% bactericidal efficacy against *P. aeruginosa*, along with high biofilm inhibition (~87%) and eradication (~80%). In a murine diabetic wound model, NBS-Lac mediates complete healing (100%) under light irradiation, significantly outperforming the controls. This work establishes carbohydrate-directed self-assembly as a novel paradigm for designing targeted, hypoxia-tolerant Type I PDT agents.

Received 12th May 2026
Accepted 5th June 2026

DOI: 10.1039/d6sc03993f

rsc.li/chemical-science

Introduction

Diabetic foot ulcer (DFU) is one of the most serious and common complications of diabetes mellitus, characterized by chronic refractory wounds.[1] These ulcers are highly susceptible to bacterial infection, which severely impedes healing. Improper management of these infected ulcers may lead to amputation. Conventional treatment typically involves the administration of antibiotics. However, the overuse and misuse of antibiotics have led to the emergence of multidrug-resistant bacteria, drastically diminishing their efficacy due to resistance.[2,3] Meanwhile, efforts to develop more potent antibiotics are accelerating the emergence of new superbugs and perpetuating a vicious cycle.[4,5] Alternative therapies like antibacterial photodynamic therapy hold a significant promise for combating bacterial infections while circumventing antibiotic resistance.

A major factor contributing to bacterial resistance is biofilm formation: bacterial communities encapsulated within an extracellular polymeric substance (EPS) matrix.[6,7] This structure not only provides physical protection to bacteria against external threats but also significantly impedes drug penetration. More critically, the hypoxia microenvironment of biofilms limits the application of conventional photosensitizers (Type II PSs).[8–10] Consequently, the development of novel oxygen-independent or minimally oxygen-dependent photosensitizer (Type I PS) system capable of effectively inhibiting and disrupting biofilms has become a pressing imperative for overcoming antimicrobial resistance. Photosensitizers are a key factor for achieving highly efficient aPDA. Enhancing the efficiency of Type-I photosensitizers centers on either blocking energy transfer from Type-II sensitizer excited states to oxygen or improving electron transfer capabilities, thereby shifting the dominant ROS generation pathway from oxygen-dependent Type-II to oxygen-independent Type-I processes.[11–13] However, the design of existing Type-I photosensitizers faces substantial challenges, often necessitating multiple components (*e.g.*, electron-donating and -withdrawing groups), which limits the generality of applicable strategies.[14–20] More importantly, their inadequate targeting capabilities and the aggregation-caused quenching (ACQ) effect induced by π–π stacking in aqueous media severely impair the generation efficiency of reactive oxygen species (particularly superoxide anion, $O_2^{\cdot-}$).[21–25] To address persistent developmental challenges in Type I

[a]*College of Chemistry and Materials Science, Key Laboratory of Medicinal Chemistry, and Molecular Diagnosis of the Ministry of Education, Hebei University, Baoding 071002, China*

[b]*State Key Laboratory of Fine Chemicals, Frontiers Science Center for Smart Materials Oriented Chemical Engineering, Dalian University of Technology, Dalian 116024, China. E-mail: sunwen@dlut.edu.cn*

photosensitizers, efficiency optimization of existing systems represents a more practical alternative.

Sulfur-substituted Nile Blue (NBS)-based photosensitizers have emerged as promising Type I photodynamic therapy (PDT) agents owing to their favorable photophysical properties. However, their therapeutic application is often hindered by suboptimal reactive oxygen species (ROS) generation efficiency and a lack of inherent targeting capability—limitations that are particularly critical in biofilm-associated infections and hypoxic microenvironments. Herein, we present glycosylated Type I photosensitizers based on a NBS scaffold, NBS-Gal and NBS-Lac. The two photosensitizers undergo spontaneous, auxiliary-free self-assembly into π-stacking-driven H-aggregates in aqueous media. This intrinsic supramolecular organization synergistically integrates molecular functionality and nanostructure, dramatically simplifying photosensitizer design. First, glycosylation promotes H-aggregation of the photosensitizers, which facilitates efficient intermolecular charge transfer and significantly elevates reactive oxygen species (ROS) generation. Notably, NBS-Lac demonstrates a greater degree of H-aggregation than both NBS-Gal and the non-glycosylated analogue NBS-NH_2, which corresponds to respective increases of 2.2-fold and 1.8-fold in the quantum yield of $O_2{\cdot}^-$ (after 4 min irradiation). Second, the photosensizers enable precise bacterial targeting through carbohydrate–lectin interactions with surface glycoproteins. As a result, NBS-Lac achieves ∼100% bactericidal efficacy against *P. aeruginosa* PA14, alongside high biofilm inhibition (∼87%) and eradication (∼80%) rates. *In vivo*, NBS-Lac mediates complete healing (∼100%) of infected diabetic wounds under irradiation, surpassing NBS-Gal (∼77%), NBS-NH_2(∼73%) and PBS controls (∼45%). Therefore, the molecular design establishes a carbohydrate-mediated supramolecular assembly mechanism that enables the integration of molecular recognition and photodynamic function within a single nanostructured system. By exploiting carbohydrate-directed H-aggregation, we demonstrate a strategy to concurrently enhance excited-state charge separation and target-specific accumulation, thereby providing a generalizable approach for constructing high-performance, hypoxia-tolerant Type I photosensitizers (Scheme 1).

Results and discussion

Molecular synthesis

The molecular design features a NBS core covalently linked to galactose (NBS-Gal) or lactose (NBS-Lac) motifs. This architecture enables spontaneous H-aggregation in aqueous media, synergistically coupling the intrinsic Type I photochemistry of the NBS core with carbohydrate-driven supramolecular assembly and active targeting. The glycosylated derivatives were synthesized *via* carboxyl-directed postmodification following established protocols,[26,27] and their structures were fully characterized by ^{1}H NMR, ^{13}C NMR, and high-resolution mass spectrometry (HRMS) (Fig. S20–34).

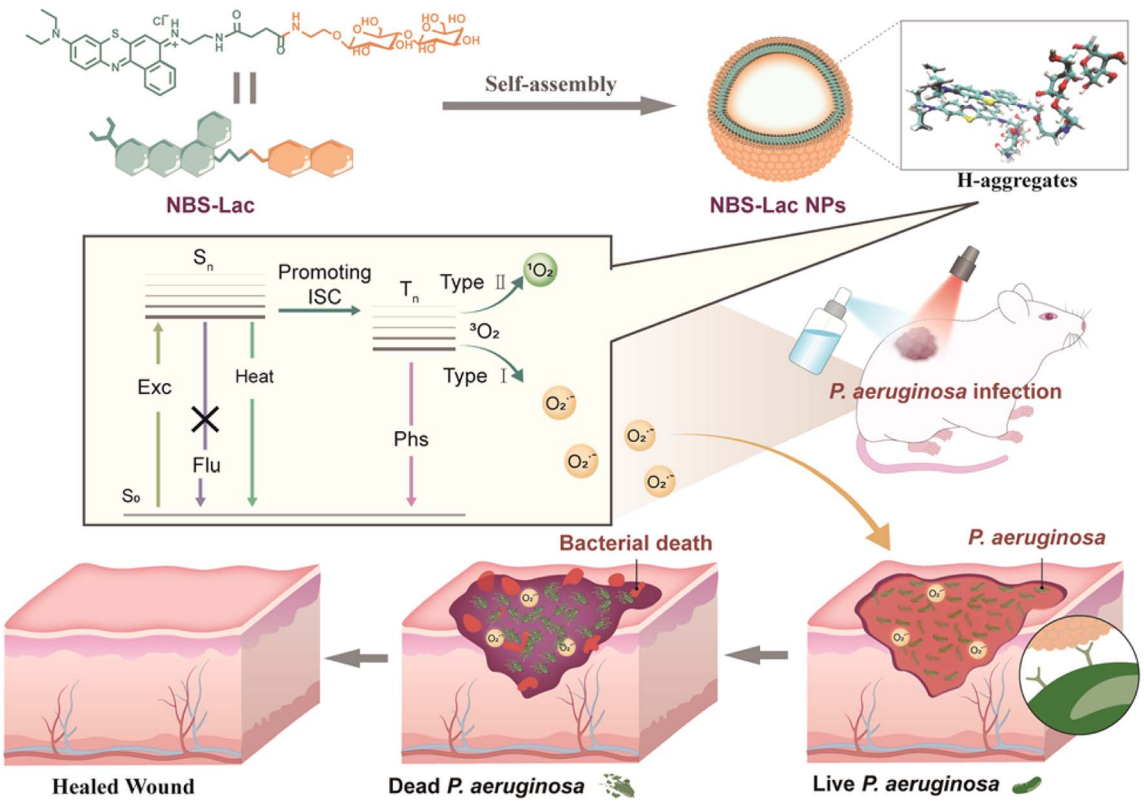

Scheme 1 Schematic illustration of glycosylation-directed H-aggregation assembly of a Type I photosensitizer into functional nanoconstructs. The resulting NBS-Lac system exhibits over 2.2-fold enhancement in superoxide anion ($O_2{\cdot}^-$) production compared to the parent photosensitizer NBS, enabled by efficient charge separation within H-aggregates for potent antibacterial photodynamic therapy (aPDT).

Self-assembly mechanisms and nanostructural characterization

Self-assembly pathways of NBS-Lac, NBS-Gal, and NBS-NH_2 were elucidated through solvent- and concentration-dependent UV/Vis absorption and fluorescence spectroscopy (Fig. 1a–c). In good solvents (DMSO/CH_3OH), all compounds exhibited a characteristic monomeric absorption band at λ_{max} ~660 nm (Fig. 1a–c). These glycosylated derivatives displayed high molar extinction coefficients ($\varepsilon \approx 7.9 \times 10^4$ M^{-1} cm^{-1}, 7.4×10^4 M^{-1} cm^{-1}, and 6.9×10^4 M^{-1} cm^{-1}), confirming potent light-harvesting capabilities. Incremental water (poor solvent) addition induced progressive attenuation of this monomer peak in NBS-Lac and NBS-Gal, with concomitant emergence of a blue shifted band at 630 nm (Fig. S2). The concentration-dependent amplification of the blue transition unambiguously signifies H-aggregation (distinct from J-aggregate signatures). Notably, H-aggregate formation was exclusive to glycosylated analogues, implicating carbohydrate moieties as critical mediators of supra-molecular ordering. The absorption peak of NBS-Lac at 630 nm is higher than that of NBS-Gal, indicating that lactose-modified NBS is more conducive to H-aggregation. Correlative TEM analyses revealed aqueous self-assembly into monodisperse nanospheres with diameters of ~100 nm (Fig. 1d and e). This well-defined nanostructure ensures excellent storage stability, retaining 90% of its initial activity after 30 days at 4 °C (Fig. S2d), and is suitable for *in vivo* application studies. Control experiments with NBS-NH_2 showed neither spectroscopic H-aggregate signatures nor nanoparticle formation, consistent with its inability to undergo carbohydrate-directed assembly.

Photodynamic properties of NBS-Lac, NBS-Gal, and NBS-NH_2

To investigate glycosylation-driven H-aggregation effects on ROS generation, we quantitatively evaluated ROS production

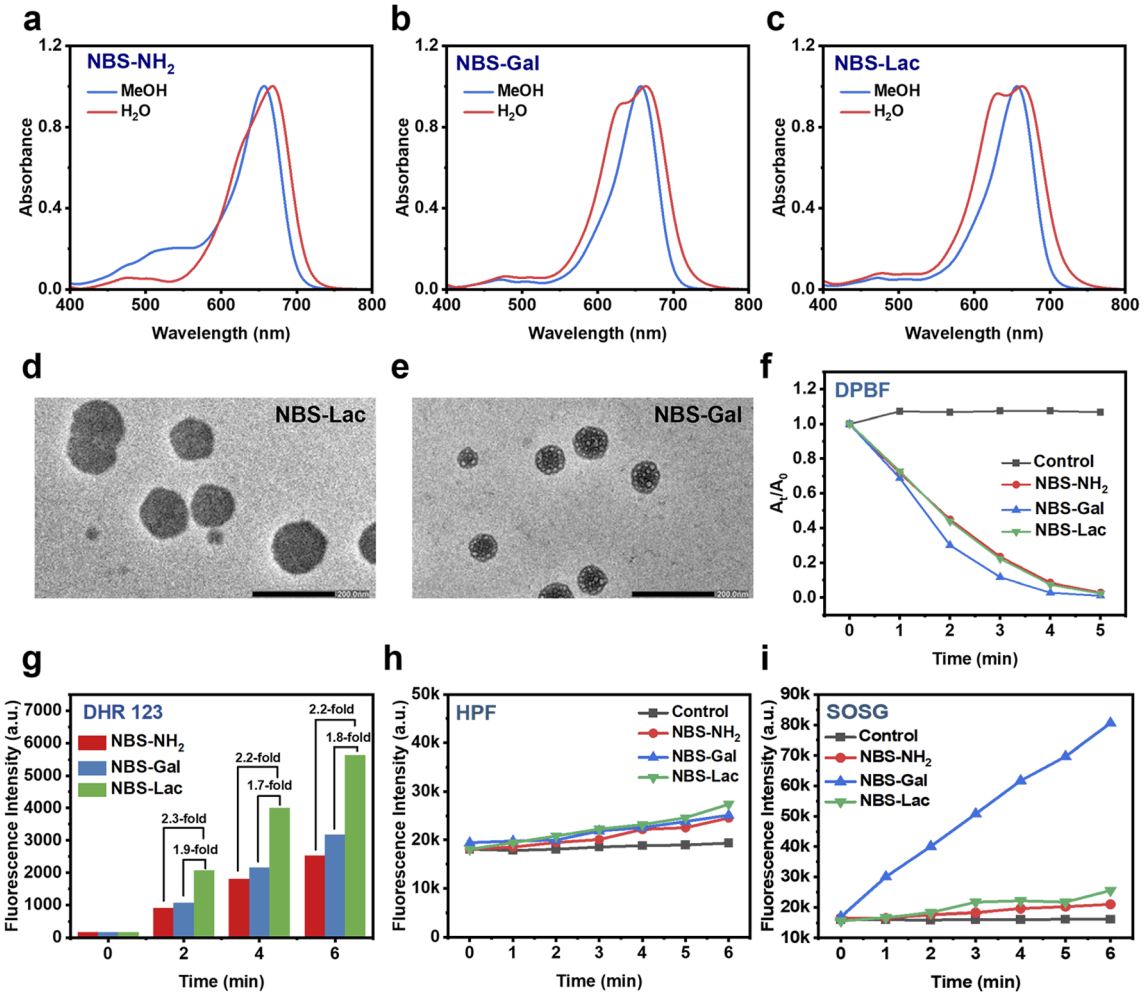

Fig. 1 (a–c) Absorption spectra of NBS-NH_2, NBS-Gal and NBS-Lac in CH_3OH and H_2O. (d and e) TEM images of NBS-Lac and NBS-Gal. Scale bar: 200 nm. (f) Photodegradation curves of 1,3-diphenylisobenzofuran (DPBF) in the presence of NBS-Lac, NBS-Gal and NBS-NH_2 in CH_2Cl_2 under light irradiation. The experiments were performed in CH_2Cl_2, where all compounds exist as monomers. (g) Maximum fluorescence intensity enhancement of DHR 123 for NBS-NH_2, NBS-Gal and NBS-Lac. (h) Maximum fluorescence intensity enhancement of HPF for NBS-NH_2, NBS-Gal and NBS-Lac. (i) Emission intensity enhancement at 525 nm of SOSG (fluorescent probe for $^1O_2$ detection, $\lambda_{ex} = 504$ nm) treated with NBS-NH_2, NBS-Gal and NBS-Lac. The abscissa represents irradiation time. The irradiation was carried out under 660 nm red LED light with a power density of 20 mW cm^{-2}.

capabilities of the monomeric and aggregated forms in solution. The singlet oxygen ($^1O_2$) quantum yields of the monomeric compounds were assessed using DPBF in CH_2Cl_2. Of note, under these conditions, NBS-Lac exists as a monomer (rather than H-aggregates); therefore, the data in Fig. 1f and S3 represent the monomeric state. These monomeric compounds showed no statistically significant differences in $^1O_2$ generation. In contrast, aqueous measurements with the SOSG probe revealed that the H-type aggregates formed by NBS-Lac substantially suppress $^1O_2$ generation (Fig. 1i and S7), confirming a clear shift from Type II to Type I photodynamic activity. Consistent with this shift, the glycosylated aggregates exhibit markedly enhanced Type I ROS production. NBS-Lac shows a 2.2-fold increase in $O_2^{\cdot-}$ generation (after 4 min irradiation) relative to non-glycosylated NBS-NH_2 (Fig. 1g and S4). Hydroxyl radical ($^{\cdot}OH$) production displayed no statistically significant difference among the three compounds (Fig. 1h and S6). ESR measurements with DMPO trapping confirmed $O_2^{\cdot-}$ photogeneration *via* characteristic DMPO–$O_2^{\cdot-}$ signals (Fig. S5), whereas no $^{\cdot}OH$ signals were detected, consistent with probe-based assays. Together, these results establish that H-aggregation in NBS-Lac may promote intermolecular charge separation and electron transfer, thereby selectively boosting Type I ROS generation.

Mechanism of promoting intersystem crossing to enhance ROS generation

To elucidate the regulatory role of glycosylation in governing the aggregation behavior of NBS, a combined molecular dynamics (MD) and theoretical computational study was conducted (Fig. 2a–f).[28,29] MD simulations revealed that glycosylation markedly alters the molecular stacking geometry: The intermolecular distance between neighboring NBS-NH_2 units was 3.19 Å, characteristic of π–π stacking, with a slip angle of ~39.57°(Fig. 2d), below the critical threshold of 54.7,[30] consistent with J-aggregation and aligning with spectral observations. In contrast, NBS-Gal dimers exhibited a slip angle of ~54.03°(Fig. 2e), suggesting coexisting J- and H-aggregation, whereas NBS-Lac displayed a slip angle of ~59.27° (>54.7°) with nearly parallel molecular planes (3.49 Å spacing), confirming predominant H-type packing (Fig. 2f). Enhanced face-to-face stacking in NBS-Lac supports its stronger H-aggregation tendency, corroborating the blue-shifted absorption near

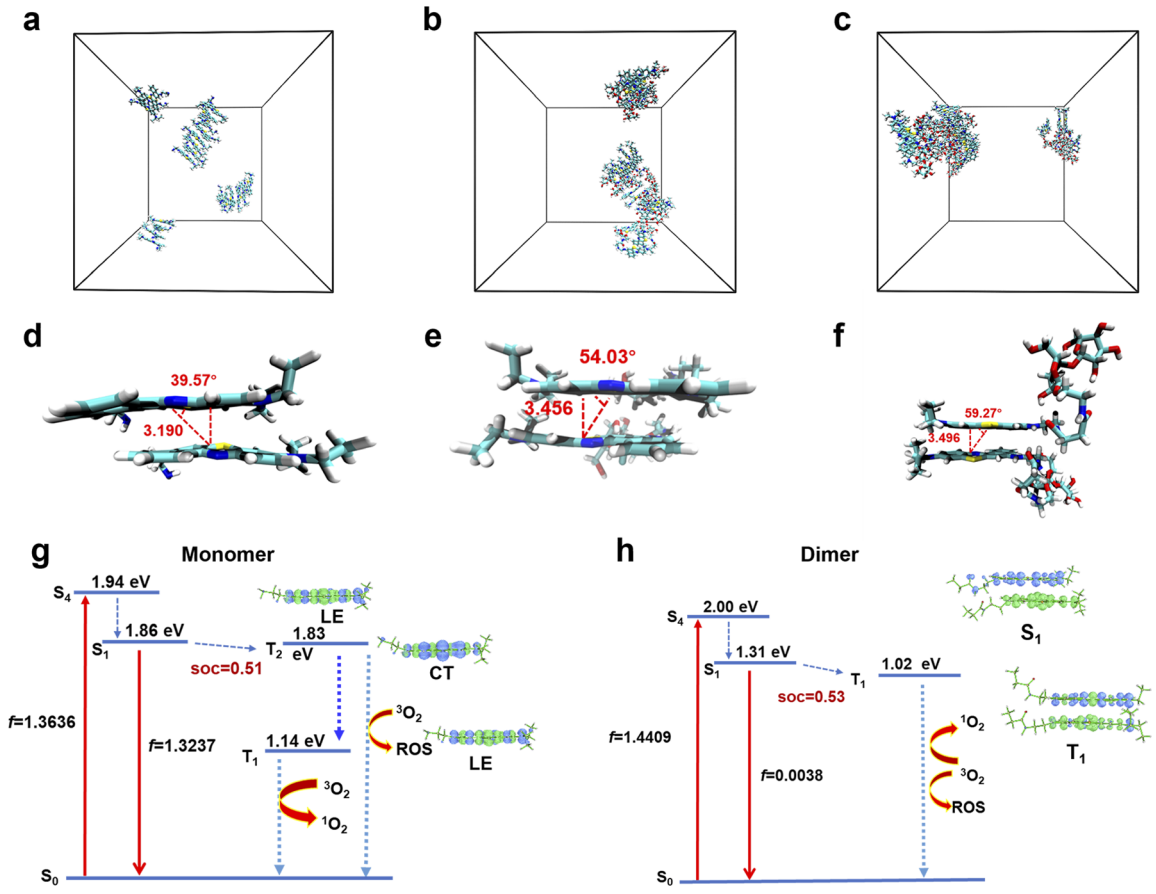

Fig. 2 Mechanism of enhancing ROS generation through promoting the intersystem crossing (ISC). (a–c) Snapshots of NBS-NH_2, NBS-Gal and NBS-Lac aggregation in water obtained by MD simulation at 298 K. (d–f) Front-view representations depicting the molecular stacking arrangement within the NBS-NH_2, NBS-Gal and NBS-Lac aggregates. The angle (θ) between the transition dipoles and the interconnected axis was measured. Generally, $\theta < 54.7°$ favors J-type aggregation, whereas $\theta > 54.7°$ favors H-type aggregation. (g and h) Schematic representation of TD-DFT-calculated energy levels, isosurfaces, and key orbital configurations for the singlet and triplet states of NBS and its coplanar dimer.

620 nm. This carbohydrate-induced face-to-face parallel alignment establishes an optimal platform for enhanced π–π interactions and efficient intermolecular charge transfer.

To gain mechanistic insight into the structure–photofunction relationship, time-dependent density functional theory (TD-DFT) calculations were performed on monomeric and dimeric NBS systems in both singlet and triplet states (Fig. 2g and h). For the NBS monomer, the lowest singlet excited state (S_1, 1.86 eV) is energetically close to the T_2 state (1.14 eV), with a small energy gap ($\Delta E_{ST} = 0.12$ eV) that facilitates efficient intersystem crossing (ISC). However, T_2 is a charge-transfer (CT) state favorable for electron transfer and radical generation. Rapid internal conversion from T_2 to T_1 subsequently populates a locally excited (LE) T_1 state with an energy >0.98 eV, which preferentially generates $^1O_2$ *via* the Type II pathway. In contrast, the NBS dimer exhibits a smaller energy gap between its lowest singlet (S_1, 1.31 eV) and triplet (T_1, 1.02 eV) states ($\Delta E_{ST} = 0.29$ eV). For the dimer, the S_1 state is characterized as a typical electron-separated state, with holes and electrons localized on separate monomer units. The triplet excited state features mixed electron-transfer (ET) and charge-separated (CS) configurations, resulting in asymmetric distribution of hole and electron densities across the two monomers. This enhanced electron separation stabilizes the excited state and facilitates electron transfer, thereby boosting ROS generation. Collectively, H-aggregation promotes Type I photodynamic activity through

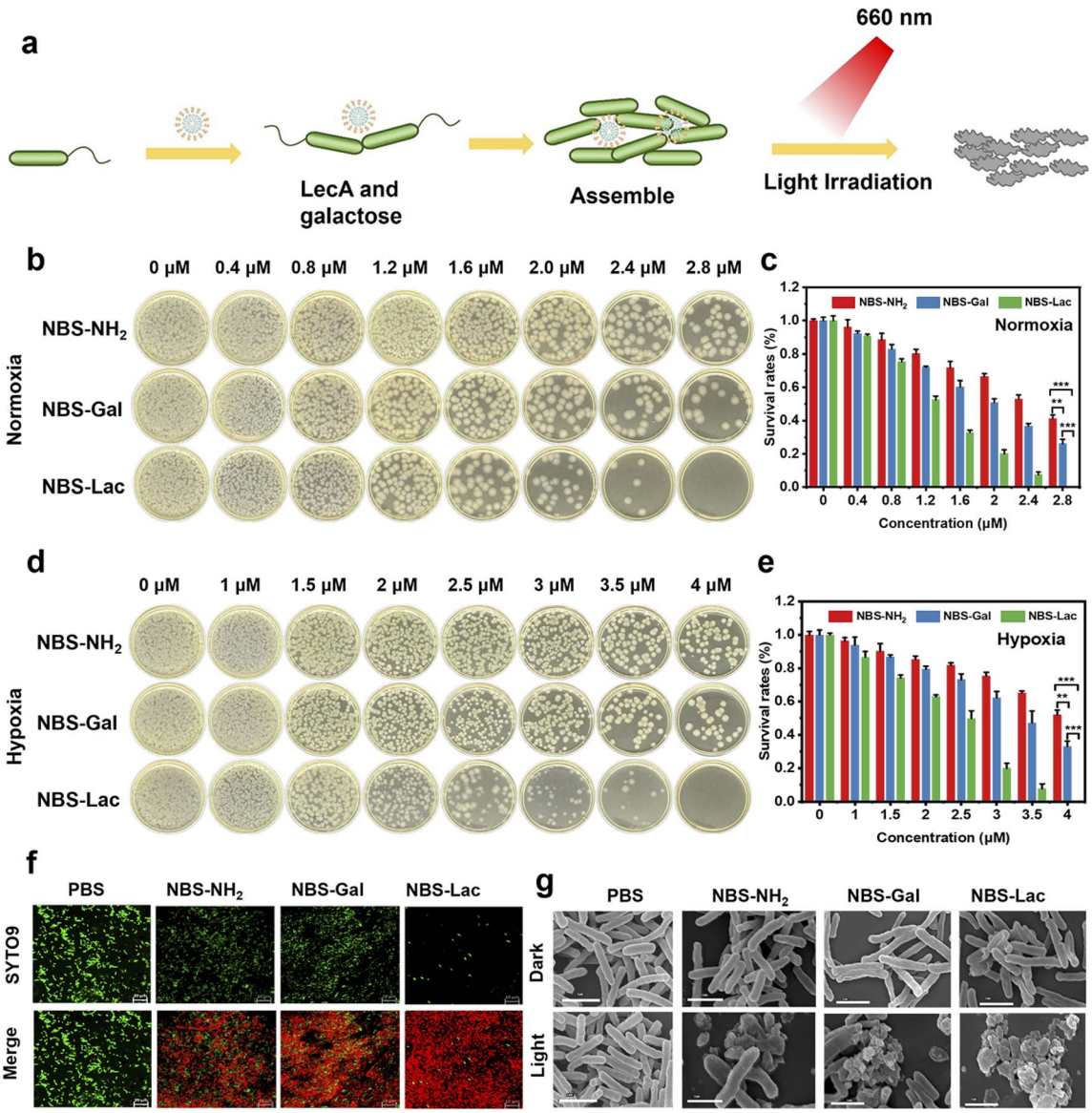

Fig. 3 (a) *In vitro* antibacterial activities of NBS-NH_2, NBS-Gal and NBS-Lac series compounds against planktonic P.A. (b) and (d) Images of P.A. colonies on LB agar plates after light treatments in normoxia and hypoxia. (c) and (e) Quantitative analysis of the bacterial cell viability based on the results of colony counting. *$p < 0.05$, **$p < 0.01$, ***$p < 0.001$ and ****$p < 0.0001$. (f) Live/dead staining of bacteria after incubation with synthetic probes. Confocal images of PA after different treatments (for SYTO9 green live bacterial stain, $\lambda_{ex} = 488$ nm and $\lambda_{em} = 500–550$ nm; for PI red dead bacterial stain, $\lambda_{ex} = 561$ nm and $\lambda_{em} = 571–630$ nm), scale bar: 10 μm. (g) Representative SEM images of P.A. stained by NBS-Lac, NBS-Gal and NBS-NH_2 after different treatments, respectively. Scale bar: 1 μm.

two distinct mechanisms compared to the monomer: (i) shifting the primary ISC pathway from S_1 to T_2 (monomer) to S_1 to T_1 (dimer); and (ii) establishing an electron-separated S_1 state and a mixed ET/CS T_1 state with enhanced electron separation, which favors electron transfer to oxygen for $O_2^{\bullet-}$ generation. These findings underscore the pivotal role of glycosylation-directed aggregation in tuning photophysical behavior and optimizing photodynamic performance, providing a mechanistic foundation for the development of next-generation hypoxia-active phototherapeutic agents.

In vitro antibacterial PDT

Capitalizing on the capacity of glycosylated-NBS derivatives to generate cytotoxic $^{\bullet}OH$ and $O_2^{\bullet-}$, we evaluated their photodynamic antibacterial efficacy against *Pseudomonas aeruginosa* PA14, a clinically relevant pathogen in diabetic wound infections. Prior to assessing antibacterial performance, we evaluated the biocompatibility of the compounds. Using MTT assays with L929 murine fibroblasts, we observed >90% cell viability after 24 h incubation with 32 μM photosensitizer, demonstrating minimal dark toxicity (Fig. S18). Hemocompatibility studies further showed less than 5% hemolysis in 4% murine erythrocyte suspensions treated with 32 μM compound (4 °C, 1 h), compared to Triton X-100 controls, confirming high biocompatibility under dark conditions for *in vivo* applications (Fig. S19). Using spread plate assays under both normoxic (21% O_2) and hypoxic (1% O_2) conditions, we observed negligible dark toxicity (>90% viability, Fig. S8a, b, S9a and b). NBS-Lac mediated PDT achieved complete bacterial eradication (100% kill rate) at 2.8 μM under normoxia, outperforming NBS-Gal and

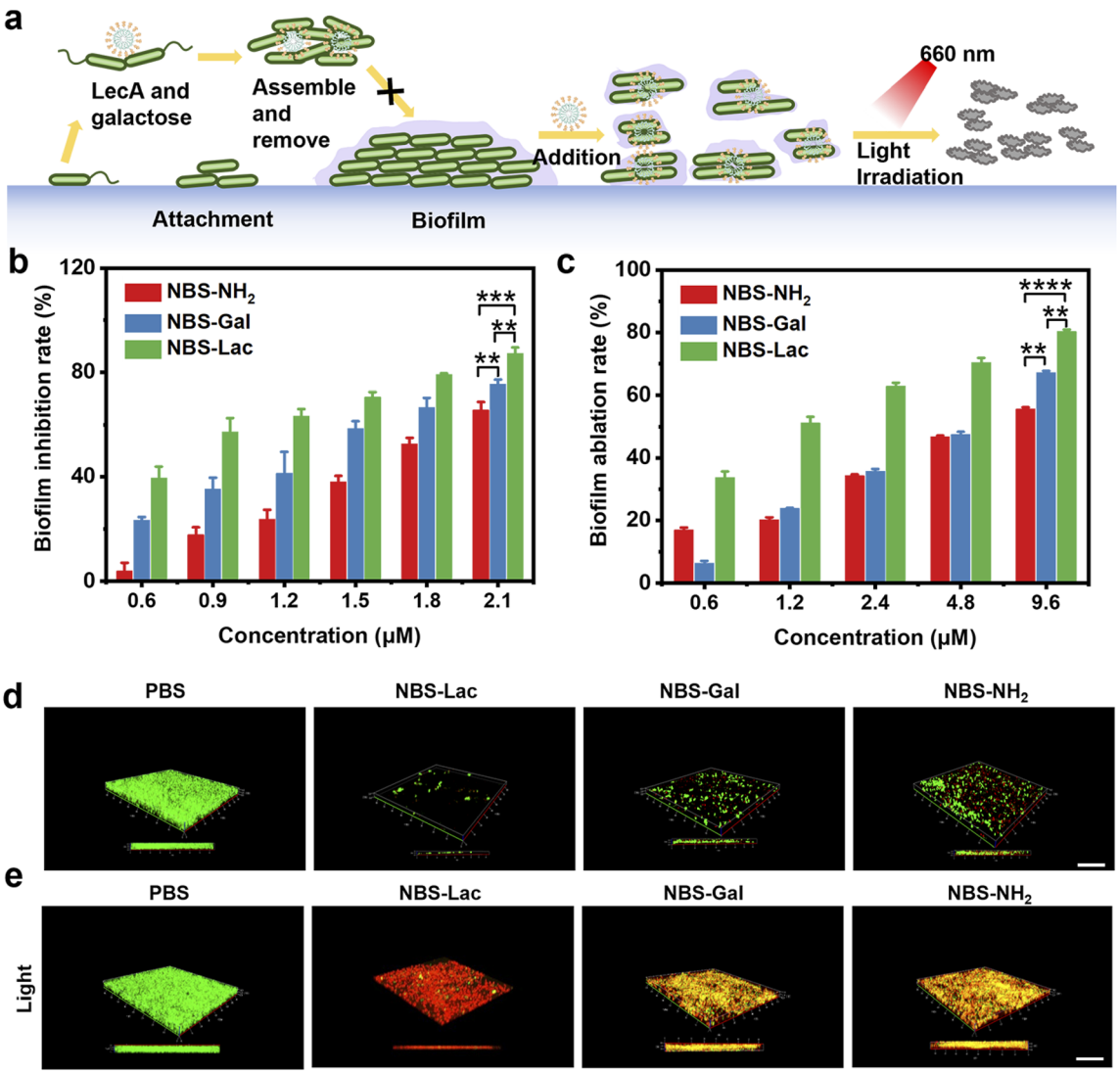

Fig. 4 The antibacterial application and the ability of NBS-NH_2, NBS-Gal and NBS-Lac to inhibit/disrupt biofilm formation. (a) Schematic illustration of the mechanism of NBS-NH_2, NBS-Gal and NBS-Lac for inhibiting the formation of bacterial biofilms. (b) Inhibition percentage of PA14 biofilm formation with various concentrations of NBS-NH_2, NBS-Gal and NBS-Lac. (c) Disruption percentage of PA14 biofilm formation with various concentrations of NBS-NH_2, NBS-Gal and NBS-Lac. (d) CLSM images of NBS-NH_2, NBS-Gal and NBS-Lac for inhibiting the formation of PA14 biofilms. Scale bar: 20 μm. (e) CLSM images of NBS-NH_2, NBS-Gal and NBS-Lac for disrupting the formation of PA14 biofilms. Scale bar: 20 μm.

NBS-NH_2, which retained ~26% and ~41% viable cells, respectively (Fig. 3b and c). Remarkably, under hypoxic conditions—where conventional photosensitizers often fail—NBS-Lac maintained complete bactericidal activity, whereas NBS-Gal and NBS-NH_2 showed substantially reduced efficacy, with survival rates of ~33% and ~52%, respectively (Fig. 3d and e). Live/dead staining and SEM further validated these results: SYTO9/PI staining showed near-total bacterial death (red fluorescence) for NBS-Lac, contrasting with residual live cells (green) in NBS-Gal/NBS-NH_2 groups (Fig. 3f). SEM revealed severe NBS-Lac-induced morphological disruption, including cell collapse and fragmentation after irradiation, exceeding damage caused by the other derivatives (Fig. 3g). To confirm the specificity of carbohydrate–lectin-mediated bacterial targeting, a competitive inhibition assay was performed using free lactose as a blocking agent. As shown in Figure S10, *Pseudomonas aeruginosa* PA14 uptake of NBS-Lac and NBS-Gal was significantly reduced—by approximately ~48% and ~27%, respectively—in the presence of excess free lactose, whereas no inhibition was observed for the non-glycosylated control (NBS–NH_2). These results confirm that the targeting is indeed mediated by specific carbohydrate–lectin interactions. The observed bactericidal activity is likely driven by both glycan-mediated bacterial recognition and lactose-enhanced H-aggregation, enabling oxygen-independent photodynamic activity that is particularly well suited for hypoxic wound therapy.

Anti-biofilm activity of NBS-Lac, NBS-Gal, and NBS-NH_2

The oxygen-independent bactericidal efficacy of NBS-Lac highlights the therapeutic advantage of this glycosylated photosensitizer in combating hypoxic wound infections. Building on its potency against planktonic *P. aeruginosa*, we evaluated NBS-Lac's capacity to combat *P. aeruginosa* biofilms—notorious for thriving in anaerobic niches and impeding treatment. The ability of NBS-Lac, NBS-Gal, and NBS-NH_2 to inhibit the formation of *P. aeruginosa* biofilms was first evaluated and quantified by crystal violet staining. Crystal violet quantification revealed that NBS-Lac (2.1 μM, 24 h incubation in the dark) reduced biofilm formation by ~88%, significantly surpassing NBS-Gal (~75%) and NBS-NH_2 (~66%) (Fig. 4b). Live/dead staining corroborated this superior biofilm–inhibitory activity (Fig. 4d). Critically, the absence of illumination implicates lactose-mediated bacterial adhesion blockade as the mechanism driving biofilm suppression rather than ROS generation. Disrupting mature biofilms poses a substantially greater challenge than inhibiting their formation, primarily due to the dense extracellular polymeric matrix that severely restricts photosensitizer penetration. To assess the anti-biofilm potential of NBS-Lac, NBS-Gal and NBS-NH_2 against pre-established *P. aeruginosa* biofilms, we administered treatments under light conditions. At 9.6 μM, NBS-Lac demonstrated remarkable efficacy in disrupting mature biofilms (~80% eradication), far exceeding the moderate effects observed with NBS-Gal (67%) and NBS-NH_2 (56%) (Fig. 4c). Consistent with these results, Live/dead fluorescence assays confirmed the potent bactericidal effect of NBS-Lac (Fig. 4e and S11). In addition, NBS-Lac treatment produced significantly thinner biofilms than those observed in the NBS-Gal and NBS-NH_2 groups. The superior disruptive efficacy is attributed to a dual-mechanism synergy: (1) cationic charge-enhanced diffusion through the biofilm matrix, and (2) glycosylation prompted the formation of H-aggregates, which significantly boosted the efficiency of ROS generation. The elevated ROS levels then degraded the extracellular polymeric matrix, enabling enhanced photosensitizer permeation and ultimately positioning it as an integrated therapeutic strategy for treating biofilm-infected hypoxic wounds.

In vivo antibacterial activity of NBS-Lac, NBS-Gal, and NBS-NH_2

Diabetic wounds have a heightened vulnerability to *P. aeruginosa* colonization and infection, significantly exacerbating the difficulty of effective treatment and presenting greater challenges for treatment control.[31] Motivated by promising *in vitro* antibacterial activity and biofilm inhibition/clearance capabilities of NBS-Lac, we evaluated the therapeutic efficacy of NBS-Lac in a *P. aeruginosa* infected diabetic rat wound model. Animals were randomized into eight groups: (1) PBS, (2) PBS + light, (3) NBS-NH_2, (4) NBS-NH_2 + light, (5) NBS-Gal, (6) NBS-Gal + light, (7) NBS-Lac, and (8) NBS-Lac + light; Additionally, three healthy rats without wound induction served as negative controls. Wound healing was monitored

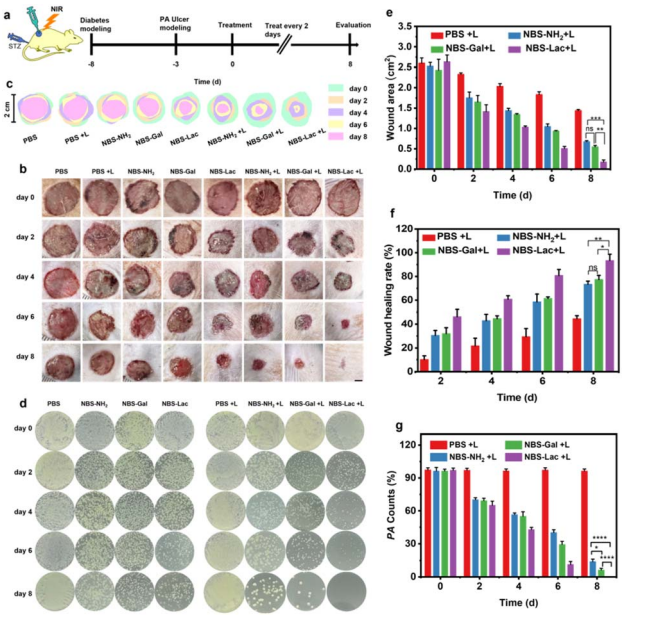

Fig. 5 The ability of NBS-NH_2, NBS-Gal and NBS-Lac to promote wound healing in PA14-infected rats *in vivo*. (a) Scheme of the therapeutic process of PA14-infected diabetic wound healing. (b) Representative images of wound change in diabetic rats infected with PA14 after different treatments. Scale bar: 4 mm. (c) Traces of wound-bed closure in diabetic rats infected with PA14 after different treatments. (d) Representative images of bacteria colonies remaining in wounds of diabetic rats infected with PA14 after different treatments. (e) Wound area changes in PA14 infected diabetic rats after different treatments. (f) Wound healing rates in PA14 infected diabetic rats after treatment. (g) Remaining bacterial counts in MDR PA infected diabetic rats after different treatments. *$p < 0.05$, **$p < 0.01$, and ***$p < 0.001$.

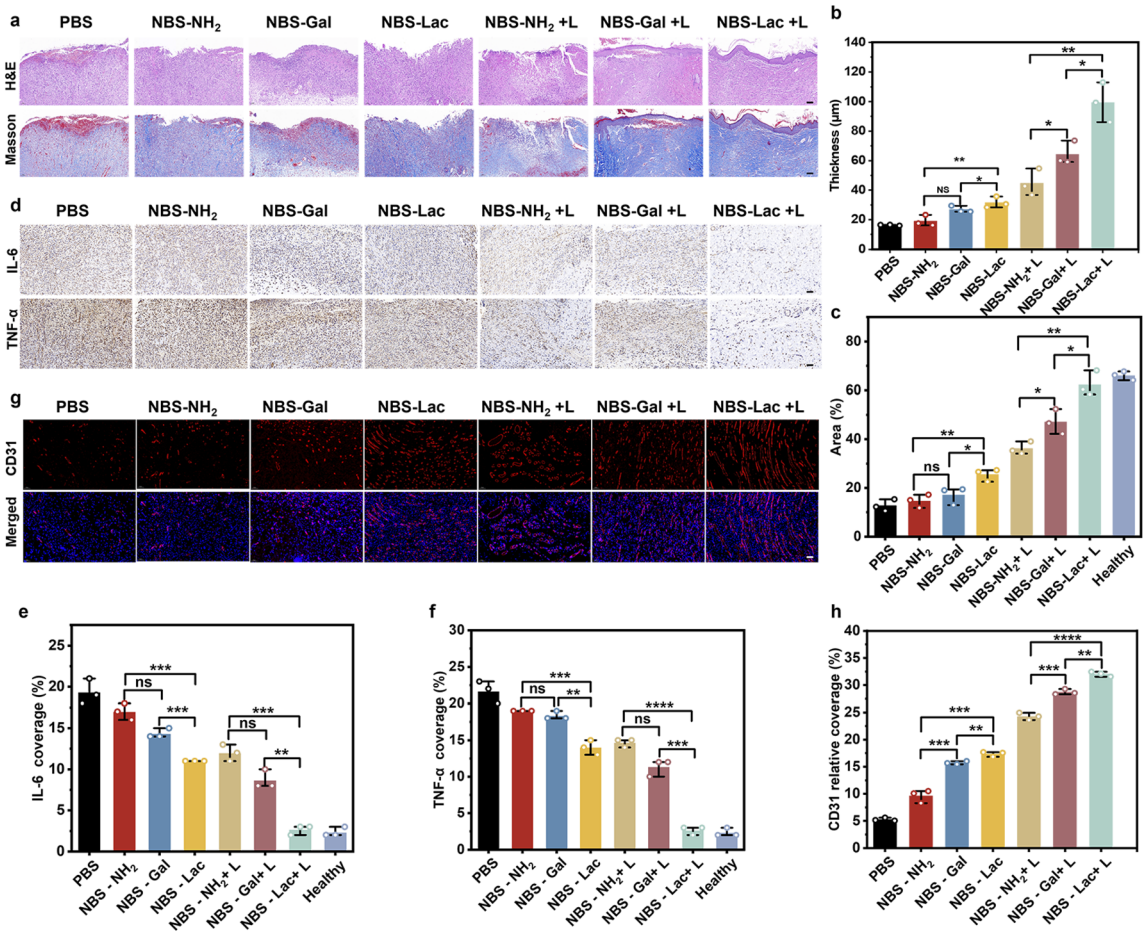

Fig. 6 (a) H&E and Masson staining of wound regeneration after various treatments on day 8. (b and c) Quantitative analysis of granulation tissue thickness and collagen deposition on day 8 post-treatment. (d) Immunohistochemical staining of TNF-α and IL-6. (e and f) Quantitative analysis of TNF-α and IL-6 in wound tissues on day 8. (g) Immunofluorescence images of CD31 staining. Scale bar was 100 nm. (h) Quantitative analysis of CD31 in wound tissues on day 8. Data are presented as mean ± SD, $n = 3$, *$p < 0.05$, **$p < 0.01$, and ***$p < 0.001$.

every two days *via* photographic documentation (closure rates) and bacterial burden analysis, alongside body weight measurements to assess systemic effects. As shown in Fig. 5b–f, the NBS-Lac + light group exhibited the highest healing rate, achieving complete wound closure by day 8, whereas ~57% of wounds in the PBS group remained unhealed. Notably, NBS-Lac achieved ~63% wound closure, suggesting that NBS-Lac can inhibit *P. aeruginosa* biofilm formation (Fig. S12 and S13). These findings are consistent with the results of the *in vitro* biofilm inhibition and clearance assays. More importantly, bacterial plate counts from infected tissue homogenates confirmed near-complete bacterial eradication in the NBS-Lac + light group, underscoring its potent *in vivo* photodynamic antibacterial activity (Fig. 5d, g and S14).

Histological analysis on day 8 post-treatment provided further evidence of the superior wound healing efficacy (Fig. 6). The NBS-Lac + light group exhibited the most advanced tissue regeneration, characterized by the thickest granulation tissue (~99 μm), a value substantially exceeding those observed in all other treatment groups, a finding further evidenced by the highest collagen deposition (~62%), approaching that of healthy skin (~65%) (Fig. 6a–c and S15a). These regenerative effects were accompanied by robust angiogenesis, as evidenced by the highest CD31 expression among all groups (Fig. 6g, h and S15c). Critically, NBS-Lac + light treatment effectively resolved inflammation, reducing TNF-α and IL-6 expression to levels comparable to those in healthy controls (2–3%), whereas PBS and non-irradiated groups exhibited persistent inflammatory responses indicative of uncontrolled infection (Fig. 6d–f and S15b). Collectively, these findings demonstrate that NBS-Lac upon 660 nm irradiation not only exerts potent antibacterial activity but also accelerates diabetic wound repair through a coordinated mechanism involving enhanced tissue regeneration, collagen deposition, inflammation suppression, and angiogenesis. *In vivo* bio-safety was confirmed by normal body weight gain (Fig. S16) and the absence of histopathological abnormalities in major organs (Fig. S17).

Conclusion

In summary, we have designed and synthesized two novel glycosylated Type I photosensitizers, NBS-Lac and NBS-Gal, which integrate bacterial targeting, enhanced $O_2^{\bullet-}$ generation, and

hypoxia tolerance within a single molecular platform. These molecules spontaneously self-assemble into H-aggregates in aqueous media *via* π-stacking, a supramolecular organization that promotes intermolecular charge transfer and facilitates intersystem crossing, leading to markedly elevated $O_2^{\bullet-}$ production. Notably, NBS-Lac exhibits 2.2-fold higher $O_2^{\bullet-}$ production (after 4 min irradiation) than its non-glycosylated counterpart, NBS-NH_2. This enhanced ROS generation translates to potent antibacterial activity under both normoxic and hypoxic conditions, effective eradication of drug-resistant *P. aeruginosa* biofilms, and accelerated healing of infected diabetic wounds *in vivo*. Comprehensive safety evaluations further underscore the translational potential of this molecular design for combating hypoxic biofilm-associated infections.

Author contributions

D. X.: design, photophysical studies, data analysis, writing – original draft, formal analysis, supervision, and funding acquisition. W. J. synthesized and characterized the fluorescent probe. M. L. designed and conducted the biological experiments and biological assays. J. G. and P. W. conducted immunohistochemical staining and analysis. Q. Y., X. F. and X. P.: validation, data analysis and review. K. W. and W. S.: methodology, formal analysis, writing, review, supervision, and funding acquisition. All co-authors wrote and edited the manuscript.

Conflicts of interest

There are no conflicts to declare.

Data availability

All experimental procedures and associated data are provided in the supplementary information (SI). Supplementary information is available. See DOI: https://doi.org/10.1039/d6sc03993f.

Acknowledgements

This research was supported by the National Natural Science Foundation of China (22408080), the Natural Science Foundation of Hebei Province (B2023201080), the State Key Laboratory of Fine Chemicals, Dalian University of Technology (KF2309), and the Foundation of Hebei University (050001-521100222046) for financial support.

References

1 J. Li, Y. Hu, B. Hu, *et al.*, *Nat. Commun.*, 2022, **13**, 627.
2 M. Baym, L. K. Stone, R. Kishony, *et al.*, *Science*, 2015, **325**, aad3292.
3 E. Brown and G. Wright, *Nature*, 2016, **529**, 336.
4 P. Klenotic, M. Moseng, C. Morgan, *et al.*, *Chem. Rev.*, 2021, **121**, 5378.
5 P. He, M. Jia, L. Yang, *et al.*, *Adv. Mater.*, 2025, **37**, 2418978.
6 D. Hu, H. Li, B. Wang, *et al.*, *ACS Nano*, 2017, **11**, 9330.
7 C. R. Arciola, D. Campoccia and L. Montanaro, *Nat. Rev. Microbiol.*, 2018, **16**, 397.
8 F. Guo, J. Yoo, Q. Zhang, *et al.*, *J. Am. Chem. Soc.*, 2025, **147**, 27932.
9 W. Chen, Y. Zhang, H. Yi, *et al.*, *Angew. Chem., Int. Ed.*, 2023, **62**, e202300162.
10 T. Xiong, F. Ning, Y. Chen, *et al.*, *ACS Nano*, 2025, **19**, 2822.
11 K. Teng, L. Niu, J. Li, *et al.*, *Angew. Chem., Int. Ed.*, 2025, **64**, e202509416.
12 V. Lechner, M. Nappi, P. Deneny, *et al.*, *Chem. Rev.*, 2022, **122**, 1752.
13 L. Zhu, X. Wang, T. Tian, *et al.*, *Chem. Sci.*, 2024, **15**, 10499.
14 K. X. Teng, D. Zhang, B. K. Liu, *et al.*, *Angew. Chem., Int. Ed.*, 2024, **63**, e202318783.
15 M. Li, Y. Xu, Z. Pu, *et al.*, *Proc. Natl. Acad. Sci. U. S. A.*, 2022, **119**, 2210504119.
16 K. X. Teng, L. Y. Niu and Q. Yang, *J. Am. Chem. Soc.*, 2023, **145**, 4081.
17 T. Xiong, Y. Chen, Q. Peng, *et al.*, *Adv. Mater.*, 2024, **36**, 2309711.
18 J. Zhuang, G. Qi, Y. Feng, *et al.*, *Nat. Commun.*, 2024, **15**, 4943.
19 X. Li, D. Lee, J.-D. Huang, *et al.*, *Angew. Chem., Int. Ed.*, 2018, **57**, 9885.
20 X. Lan, H. Li, Y. Liu, *et al.*, *Angew. Chem., Int. Ed.*, 2024, **63**, e202407092.
21 J. Liu, D. W. Kang, Y. Fan, *et al.*, *J. Am. Chem. Soc.*, 2024, **146**, 849.
22 M. Li, J. Xia, R. Tian, *et al.*, *J. Am. Chem. Soc.*, 2018, **140**, 14851.
23 Z. An, C. Zheng, Y. Tao, *et al.*, *Nat. Mater.*, 2015, **14**, 685.
24 T. J. Penfold, E. Gindensperger, C. Daniel, *et al.*, *Chem. Rev.*, 2018, **118**, 6975.
25 Z. Wang, W. Ma, Z. Yang, *et al.*, *J. Am. Chem. Soc.*, 2024, **146**, 28973.
26 Y. Chen, T. Xiong, Q. Peng, *et al*, *Nat. Commun.*, 2024, **15**, 6935.
27 J. Yang, F. Yin, H. Li, *et al*, *Adv. Healthcare Mater.*, 2025, **14**, 2404859.
28 D. Xi, M. Xiao, J. Cao, *et al*, *Adv. Mater.*, 2020, **32**, 1907855.
29 D. Xi, N. Xu, X. Xia, *et al*, *Adv. Mater.*, 2022, **34**, 2106797.
30 C. Sun, B. Li, M. Zhao, *et al*, *J. Am. Chem. Soc.*, 2019, **141**, 19221.
31 J. Makabenta, A. Nabawy, C. Li, *et al*, *Nat. Rev. Microbiol.*, 2021, **19**, 23.